Permeability and elastic properties of cracked glass under pressure

A. Ougier-Simonin,[1] Y. Guéguen,[1] J. Fortin,[1] A. Schubnel,[1] and F. Bouyer[2]

Received 29 October 2010; revised 29 March 2011; accepted 15 April 2011; published 12 July 2011.

[1] Fluid flow in rocks is allowed through networks of cracks and fractures at all scales. In fact, cracks are of high importance in various applications ranging from rock elastic and transport properties to nuclear waste disposal. The present work aims at investigating thermomechanical cracking effects on elastic wave velocities, mechanical strength, and permeability of cracked glass under pressure. We performed the experiments on a triaxial cell at room temperature which allows for independent controls of the confining pressure, the axial stress, and pore pressure. We produced cracks in original borosilicate glass samples with a reproducible method (thermal treatment with a thermal shock of 300°C). The evolution of the elastic and transport properties have been monitored using elastic wave velocity sensors, strain gage, and flow measurements. The results obtained evidence for (1) a crack family with identified average aspect ratio and crack aperture, (2) a very small permeability which decreases as a power (exponential) function of pressure, and depends on (3) the crack aperture cube. We also show that permeability behavior of a cracked elastic brittle solid is reversible and independent of the fluid nature. Two independent methods (permeability and elastic wave velocity measurements) give these consistent results. This study provides data on the mechanical and transport properties of an almost ideal elastic brittle solid in which a crack population has been introduced. Comparisons with similar data on rocks allow for drawing interesting conclusions. Over the timescale of our experiments, our results do not provide any data on stress corrosion, which should be considered in further study.

Citation: Ougier-Simonin, A., Y. Guéguen, J. Fortin, A. Schubnel, and F. Bouyer (2011), Permeability and elastic properties of cracked glass under pressure, *J. Geophys. Res.*, *116*, B07203, doi:10.1029/2010JB008077.

1. Introduction

[2] Cracks in rocks are of critical importance because rock elastic and transport properties [*Walsh*, 1965; *Brace et al.*, 1968] depend on them. For that reason, they play a key role in fault mechanics (earthquakes) and in many geotechnical issues (stability of boreholes, stimulation of oil and geothermal reservoirs, the design of tunnels and nuclear waste disposals). Numerous studies of crack effects in rocks have been conducted in the past [*Scholz*, 1968; *O'Connell and Budiansky*, 1974; *Brown and Korringa*, 1975; *Kranz*, 1983; *Paterson and Wong*, 2005]. Some of these investigations have reported the crack effect on elastic wave velocity and permeability properties associated with increasing pressure, for instance in granite [*Pratt et al.*, 1977; *Kranz et al.*, 1979; *Benson et al.*, 2006a, 2006b; *Nasseri et al.*, 2009], and in basalt [*Vinciguerra et al.*, 2005; *Benson et al.*, 2006b; *Fortin et al.*, 2010; *Nara et al.*, 2010]. Originally however, cracks were investigated in glass. The pioneering work of *Griffith* [1920] has been indeed the first step in building up the theoretical framework of Fracture Mechanics [*Lawn*, 1993].

[3] Glass is an almost ideal isotropic linear elastic solid. It thus provides a useful reference when compared to rocks. Since the work of Griffith, many studies have investigated the damage and the cracking in glass through various experimental, theoretical and, recently, numerical approaches. Some of these studies particularly focused on slow crack growth and stress corrosion processes [*Wiederhorn*, 1966; *Anderson and Grew*, 1977; *Atkinson and Meredith*, 1987]. Most of the experimental investigations have been conducted using extensional stresses and, to our knowledge, none considered crack evolution under compressive stress. Some of this work explored thermal crack propagation in glass under tension conditions [*Adda-Bedia and Pomeau*, 1995; *Sakaue et al.*, 2009]. The vitrification process used for nuclear waste disposal and geological disposal has also motivated some thermal cracking investigations in glass [*Perez and Westsik*, 1981; *Sato et al.*, 1983; *Kamizono and Senoo*, 1983; *Falleti and Ethridge*, 1988]. All of these investigations were conducted with zero confining pressure.

[4] Investigating cracks in glass under pressure is of interest for two reasons. First it can provide data on crack behavior in an almost ideal brittle elastic solid, providing a simplified system that can be compared to real rocks. Understanding how cracks modify elastic and transport properties can help to understand similar effects in more complex rocks. Second, it is of direct interest to nuclear waste disposal, since radioactive waste is vitrified in glass cylinders.

[1] Laboratoire de Géologie, Ecole Normale Supérieure, CNRS, UMR 8538, Paris, France.
[2] CEA, Site de Marcoule DTCD/SECM, Bagnols-Sur-Cèze, France.

0148-0227/11/2010JB008077

Table 1. Principal Elastic Parameters Measured in Ambient Conditions in the Original SON68 Glass (No Thermal Treatment) and in a 300°C Thermally Treated One (TT300 Glass)

Elastic Parameters	Original Glass	TT300 Glass
ρ	2.8	2.8
V_P (m/s)	5970 ± 30	4500 ± 90
V_S (m/s)	3380 ± 30	1980 ± 90
K (GPa)	56.2 ± 4	50.3 ± 3
G (GPa)	32.8 ± 1	11.2 ± 2
E (GPa)	83.6 ± 2	31.2 ± 3
ν	0.27 ± 0.03	0.39 ± 0.01

Recently, *Ougier-Simonin et al.* [2010] presented some results on the mechanical and elastic properties obtained on a dry cracked synthetic glass (SON68) under pressure.

[5] In this study, we investigated thermomechanical cracking effects on elastic wave velocities, mechanical strength and permeability under pressure. We present first the samples and the experimental methods. Then the data obtained for mechanical properties and permeability are reported. The results are discussed and interpreted using damage and permeability models.

2. Samples and Experimental Methods

2.1. Sample Characterization

[6] The glass matrix is amorphous, as expected, with isotropic properties. We measured elastic wave velocities under ambient conditions of room temperature and atmospheric pressure to determine the reference values for the elastic moduli. The data are summarized in Table 1. The chemical composition of the investigated glass SON68 is very close to the composition of the borosilicate glass used to immobilize high-level nuclear waste in France [*Frugier et al.*, 2008]. Platinoids (ruthenium and paladium) have been included in the glass matrix to simulate the presence of radionuclides of active glasses. They form insolubles (aggregates, clusters or needles) homogeneously spread within the glass matrix as can be seen on Figure 1 (blank minerals).

2.2. Thermally Induced Cracks

[7] The starting original material is produced in ideal conditions of slow cooling that prevents any crack formation. Thereby, we developed a protocol to create cracks within the material by a thermal shock in a reproducible way. A previous study of quench effects in a different borosilicate glass has shown that there exists two critical temperatures for this type of material [*Kamizono and Senoo*, 1983]. Cracks first appear after quenching from a threshold temperature, which was 74°C with the *Kamizono and Senoo* [1983] borosilicate glass, and brittle failure around a second threshold temperature which was ~600°C with their borosilicate glass. Our glass (SON68) is different and its melting point occurs at T = 512°C. Consequently we have heated this SON68 glass to a maximum temperature of 300°C for quenching. All samples have been heated with a furnace (Thermolyne 1400 furnace Sybron©), with an uncertainty in temperature of ±1°C. An external thermocouple has been added to monitor the temperature of the sample surface. Temperature was incremented at the rate of 3°C per minute, up to the maximum chosen heating temperature T_H. The sample was left for 15 hours at T_H, then quenched in less than 5 seconds into distilled water at room temperature T_A = 20°C. The thermal shock leads to a differential stress field and stress relaxation inducing crack creation and propagation.

[8] The cracks produced by the thermal treatment are very thin and segmented. They propagate in short straight segments or they are smoothly curved up (Figure 1). The highest crack density should be observed on the sample surface however it remains almost equivalent in all the material. Consequently, our first assumption is to consider a homogeneous crack distribution in our thermally treated samples. Additionally, we could not clearly identify the origin of the cracks from these pictures but they seem to be independent from the platinoid presence.

[9] The crack porosity created by the thermal treatment was measured with a mercury porosimeter. Crack porosity of a 300°C thermally treated glass is about 0.24%. The pore size distribution (Figure 2) shows three main peaks, at around 1 μm, 10 μm, and beyond 10^2 μm. The latter crack family accesses the air bubbles trapped in the matrix and surface cracks. This is believed to include sample surface artifacts related to the maximum thermal shock. These large radii correspond to values much higher than those controlling the pressure dependence, as discussed in section 4.3.

[10] The dotted line on the Figure 2 represents the porosity distribution. As for the original sample, elastic wave velocities have been measured in thermally treated (TT) glass samples (Table 1). As expected, the velocities are lower in the cracked glass than in the original glass, due to the presence of cracks [*Walsh*, 1965].

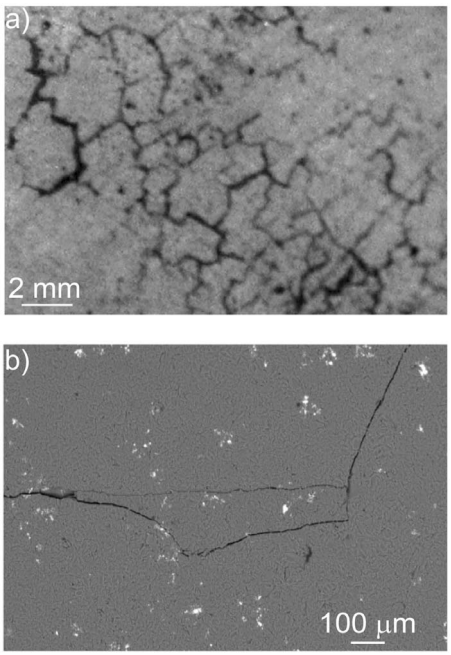

Figure 1. Cracks induced by thermal treatment in the SON68 synthetic glass. Picture of cracks (a) on glass surface (surface photography of a glass cylinder sample TT at 300°C) and (b) SEM-BSE radial section (middle of the cylinder) ×320 (blank minerals are platinoids).

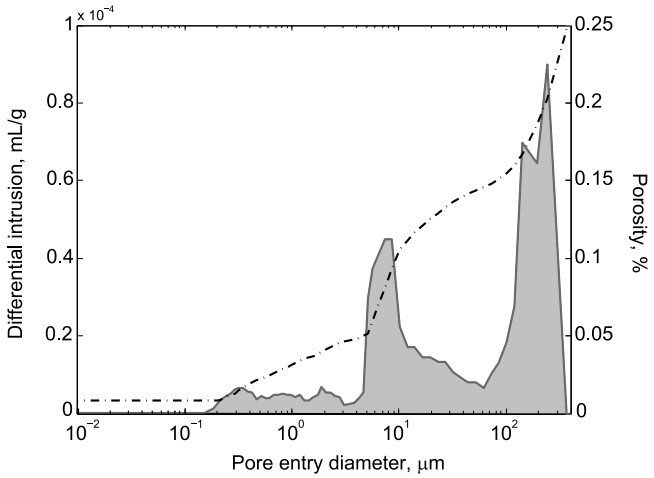

Figure 2. Porosity of a thermal treated glass at 300°C. Grey surface displays the crack size and air bubble distribution.

2.3. Numerical Modeling of Thermally Induced Stresses

[11] We used a finite element code to model the temperature effect on stress distribution during the quenching performed at T_{max} = 300°C. This gives us an estimate of the global crack orientation resulting from the stresses induced by quenching. The model uses the finite difference method, in three dimensions and in an elastic field. First, we selected a representative 3D surface in our cylinder in order to have an efficient mesh, taking into account the symmetry axis. This reduces the modeled surface to a rectangular surface of 4 × 2 cm, and we assume that it is representative of the sample. The mesh is of 50 × 50 Lagrange node elements (where the basic functions are equal to 1 at one node and 0 at others) for a Gaussian quadrature 2 × 2. Second, we introduced the Fourier heat equation for a source term equal to zero (no energy produced) such as

$$\lambda \nabla^2 T = \rho C_p \frac{\partial T}{\partial t}, \tag{1}$$

where T is temperature in °C and t is time in seconds. The synthetic glass density, ρ is 2850 kg m^{-3}, the specific heat, C_p, is about 801.6 J kg^{-1} °C^{-1}, and the thermal conductivity, λ, is around 0.7 W m^{-1}°C^{-1}. To solve equation (1), we need a boundary condition on temperature at the border of the glass as a function of time. Thus, we measured the temperature evolution on the glass surface during one quenching, from inside the furnace to 2 hours after the quenching. These data are given in Table 2.

[12] Using equation (1) and the boundary conditions (Table 2), we can calculate the temperature field in the glass and, as a consequence, the stress field induced in an elastic model using

$$\sigma_{ij} = C_{ijkl}\varepsilon_{kl} - 3K_o\alpha\Delta T\delta_{ij}, \tag{2}$$

where K_o is the bulk modulus of the original glass in GPa (Table 1), σ_{ij} the stress, C_{ijkl} the elastic tensor and ε_{kl} the strain. δ_{ij} is the Kronecker symbol. The coefficient of thermal expansion of our glass is $\alpha = 8.3\ 10^{-6}$ ° C^{-1}.

[13] Figure 3 shows the temperature and the stress fields at 20 s after the thermal shock. The stresses are given in cylindrical coordinates where σ_{rr} is the radial stress, $\sigma_{\theta\theta}$ the horizontal tangential stress and σ_{zz} the vertical stress. Given the geometry and slenderness of the sample, the thermoelastic field can be approximated by the plane strain solution for a solid cylinder (as discussed by, e.g., *Timoshenko and Goodier* [1970], section 151), except in the vicinity of the top and bottom surfaces. The quenching was sufficiently rapid that the analytic solution for an instantaneous change of temperature on the surface would be adequate, which is corroborated by the numerical simulations in Figure 3. Thus, the analytical solution can potentially provide several useful insights into the spatial and temporal development of thermally induced damage. First, the maximum hoop stress is to be found near the surface very early in the quenching process, with magnitude

$$\sigma_{\theta\theta} = \frac{\alpha E \Delta T}{1-\nu} \approx 250\text{MPa} \tag{3}$$

for the thermoelastic parameters in this study. The magnitude of this tensile stress decreases with time. Second, this stress is tensile within an external ring of 3 − 4 mm of thickness (Figure 3), but compressive within a cylindrical core, with a time-dependent radius that can be quite large depending on the thermoelastic properties. Third, the axial stress can also be tensile, but with magnitude smaller than the hoop stress. The radial stress is compressive, increasing in magnitude from 0 (at the surface) to reach a plateau in the interior. It appears that 20 s after the thermal shock, the stress values are maximum and the stress distribution is representative of the thermally induced damage in our experiments. From Figure 3, $\sigma_{\theta\theta} > \sigma_{rr}$ and $\sigma_{\theta\theta} > \sigma_{zz}$, thus we can predict that the main orientation of the crack population is mainly subvertical (i.e. mainly parallel to the z direction).

2.4. Experimental Setup

[14] Three triaxial experiments have been conducted on thermally treated glass samples, in dry and saturated (argon, water) conditions. These experiments were performed using a triaxial cell installed in our laboratory at Ecole normale supérieure in Paris (Figure 4). This apparatus (Figure 4a) allows for (1) hydrostatic pressure ([0;100] MPa), (2) deviatoric load ([0;700] MPa), and (3) pore pressure ([0;100] MPa) to be applied independently on a cylindrical specimen of 40 mm in diameter × 80 mm in length. Room temperature is controlled with an accuracy of ±0.5°C around 20°C.

Table 2. Temperatures Measured on the Synthetic Glass Sample Surface During a Thermal Shock Performed at 300°C

Time	Temperature (°C)
t_o = 0 s	300
5 s	42
10 s	40
20 s	38
5 min	40
2 h	32

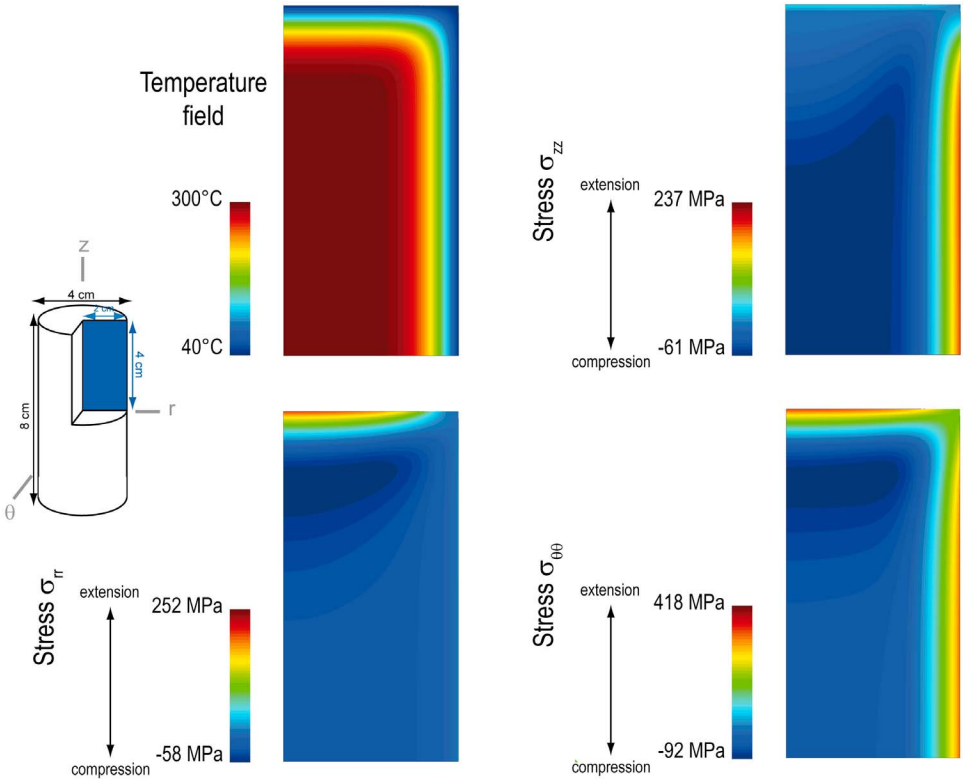

Figure 3. Modeling of the temperature field and stress spatial distribution of a 300°C TT glass quenched for 20 s. Here σ_{rr} is the radial stress, $\sigma_{\theta\theta}$ is the horizontal tangential stress, and σ_{zz} is the vertical stress.

[15] Sixteen ultrasonic piezoelectric transducers for elastic wave velocity measurements (V_P and V_S) were glued on each sample (Figure 4b), using coaxial connections through the wall of the cell pressure chamber. The control and data acquisition were performed by dedicated softwares (Falcon ST© for pressure and strain controls, InSite ASC© Ltd. for elastic wave velocity measurements). Strain measurements were acquired with 8 strain gages (4 axial and 4 circumferential, Figure 4b) and monitored by an external gap sensor using Foucault currents (Figure 4a) which provides, once corrected, a global axial strain measurement. These data were used to correct the elastic wave velocity raypath from the sample axial and radial deformation. Further details on the experimental setup can be found in the work of *Ougier-Simonin et al.* [2010].

[16] The pore pressure was generated by a QuiziX© pump with 2 cylinders. This apparatus allows for an independent control of the cylinders, and so, for a differential control of the fluid flow at the sample bases (Figure 5). Using the constant flow method, we applied a different pore pressure value on each cylinder to create a pressure gradient $\Delta P/L$ following Darcy's law (Figure 5a):

$$\frac{Q}{S} = \frac{k}{\mu}\frac{\Delta P}{L}, \tag{4}$$

where Q is the fluid flow ($m^3.s^{-1}$), S the sample area (m^2), L the sample height, and μ is the dynamic viscosity of the fluid (Pa.s). However, this method can only measure the permeability for $k \geq 10^{-18}$ m^2. As the porosity of our cracked glass is very low, we considered a second method to explore lower permeability.

[17] Following the pulse decay method of *Brace et al.* [1968], for $k < 10^{-18}$ m^2, we applied a transient pressure pulse on one cylinder while fixing the fluid pressure of the second cylinder. This allowed us to measure the fluid diffusion through the sample and its exponential decay with time until pressure equilibrium was reached in the sample, according to

$$k = a\mu\beta\frac{L}{S}\left(\frac{1}{\frac{1}{V_A}+\frac{1}{V_B}}\right), \tag{5}$$

with

$$P_A - P_f = \Delta P_o \frac{V_A}{V_A + V_B} e^{-at}. \tag{6}$$

V_A and V_B (m^3) are the cylinder reservoir volume of the pore pressure pump, respectively, (including the volume of the connecting tubes). P_A is the pressure applied to the V_A volume injected in the sample and P_f is the final pressure when the equilibrium state is reached. ΔP_o is the initial pressure increment and β is the isothermal incompressibility coefficient of the injected fluid (Pa^{-1}). We calculate the exponential coefficient a from the plotted experimental data in a semi-logarithmic scale.

[18] This method was partly realized in our experiments. As each measurement took several hours to several days to be

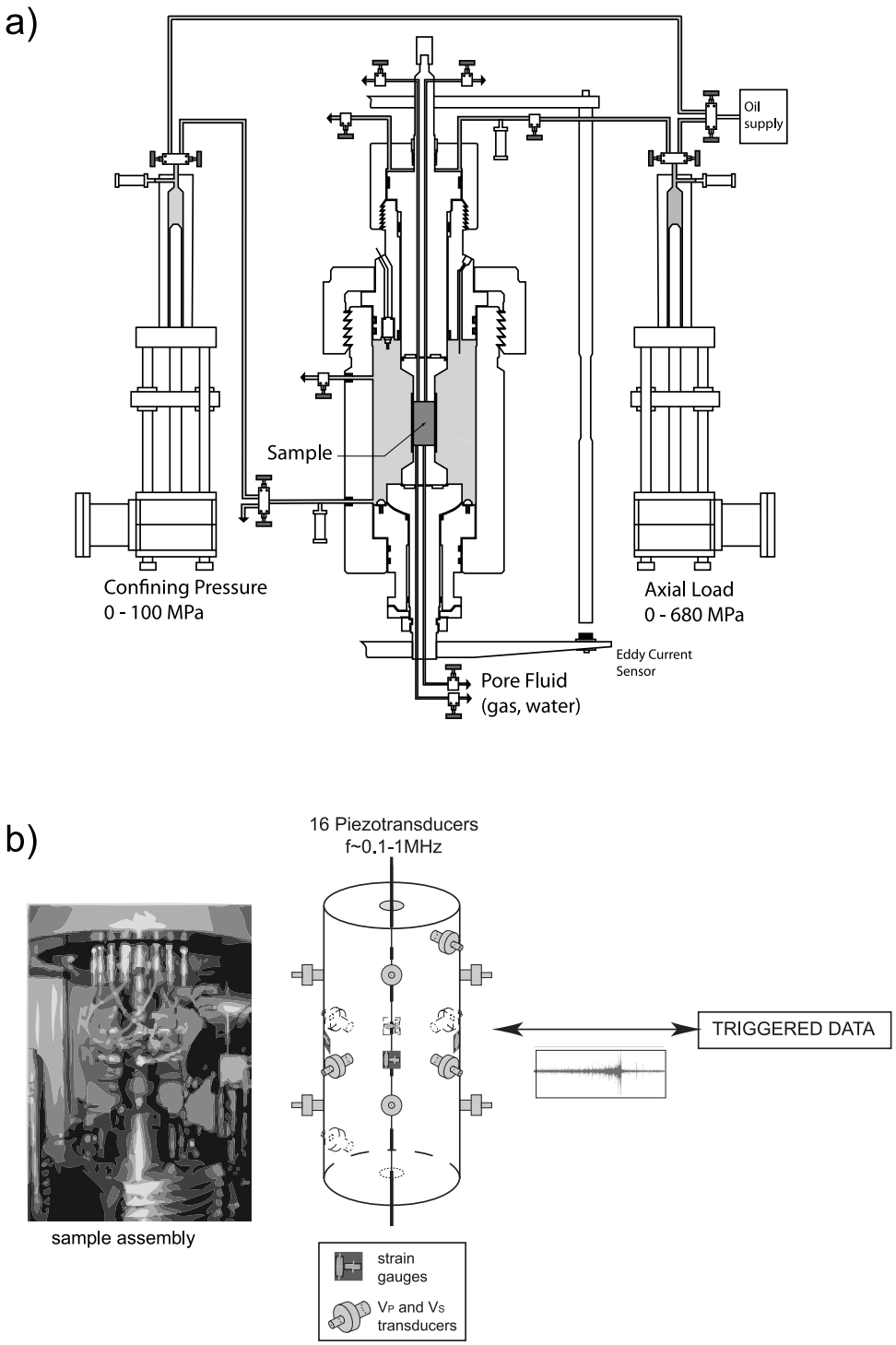

Figure 4. Scheme of (a) the triaxial cell apparatus at Ecole Normale Supérieure and (b) monitoring setup and sensor arrangement on a sample.

obtained, we modified the approach above according to *Bernabé* [1987] so that the decay of the pressure transient occurred more rapidly. Thus equation (5) is simplified into equation (7), V_{pulse} being the total fluid volume (cylinder + tubes):

$$k = a\mu\beta\frac{L}{S}V_{pulse}. \tag{7}$$

Note that $V_{pulse} = V_A$ or V_B, depending on whether the pressure increment is applied on the cylinder V_A or on the cylinder V_B. The total tube volume is about 0.3 μL.

[19] We performed one experiment using argon gas and one using Vittel mineral water (commercially available, with known and stable chemical composition). As the gas flow could be affected by the rugosity of narrow pipes (such as crack edges), we fixed the pore pressure value to 5 MPa for

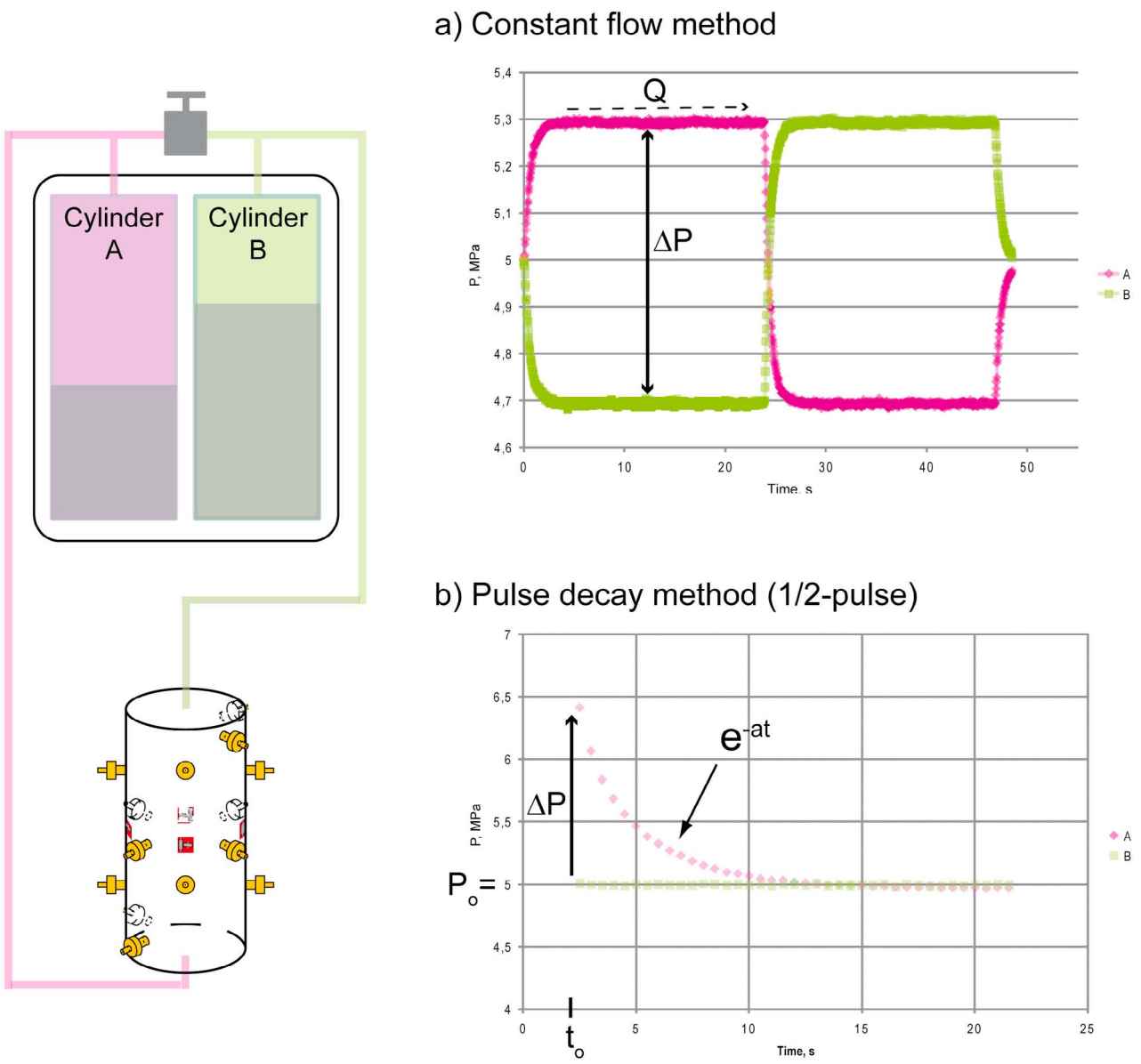

Figure 5. Pore pressure schematic setup and plots of the two types of permeability measurements.

both the argon gas and water experiments. Following *Spiers et al.* [1984], the effective permeability does not vary significantly at this pore pressure which allows us to neglect the Klinkenberg effect. Indeed, under these conditions, the mean free path of the argon molecules is calculated to be $\lambda \sim$ nm [see *Gueguen and Palciauskas*, 1994], so that $\lambda \ll$ pore size, implying that the Klinkenberg correction is negligible.

[20] All the tests were performed applying the same loading path from 0 to 25 MPa hydrostatic pressure at 0.01 MPa/s with steps of 2.5 MPa. Elastic wave measurements were measured at each pressure step, before and after the permeability measurements. Strain data were continuously recorded to allow us to correct our velocity data for the sample deformation. For the argon gas saturated test, the unloading path was decreased hydrostatically from 25 to 15 MPa. Then, the confining pressure was fixed to 15 MPa and the axial stress was increased to 190 MPa at a constant strain rate of 10^{-6} s^{-}1. For the water saturated test, the unloading path was decreased hydrostatically from 25 to 0 MPa.

3. Experimental Results

3.1. Elastic Wave Velocities in Saturated Cracked Glass

[21] Figure 6a shows the elastic wave velocity data measured in the two saturated samples. The velocity data for each sample are the average values calculated from the 16 sensors glued on the lateral surface of the glasses. Below 7 MPa effective pressure, the measurements have an error that decreases from 2.5% to 1%. This error represents both the intrinsic uncertainty of the measurements and the dispersion of the velocities induced by the crack presence. This disper-

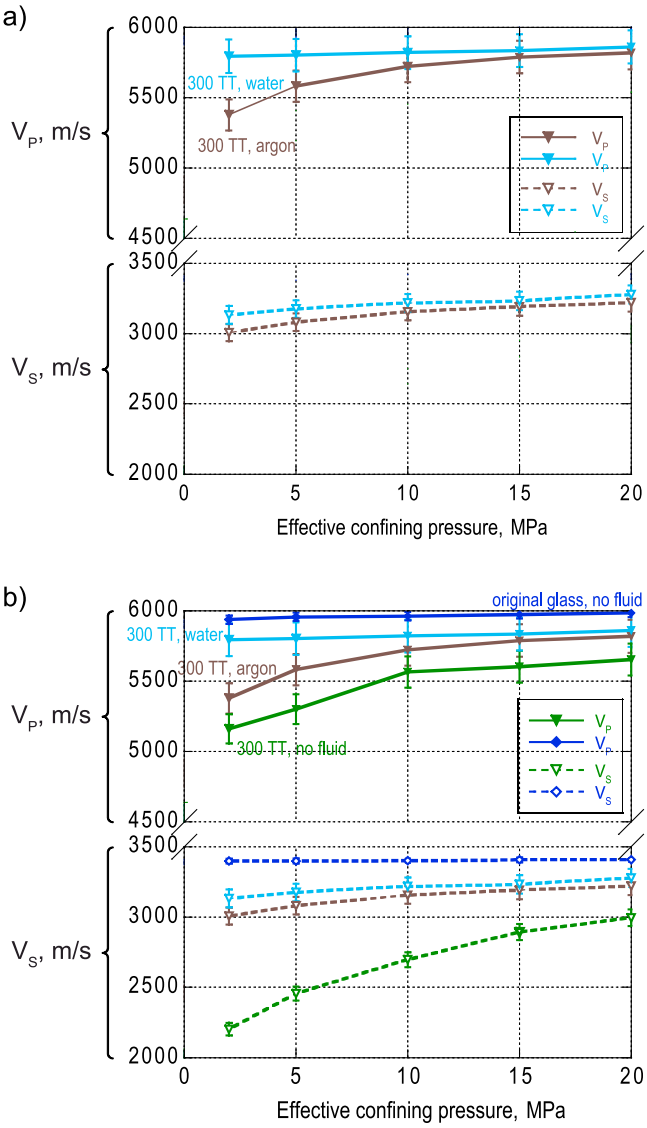

Figure 6. (a) Average evolution of the elastic wave velocities measured in the saturated glasses (argon gas in brown and water in blue) under hydrostatic conditions. (b) The data are compared with the elastic wave velocities measured in a dry thermally treated glass and in the original glass. The error on each value is estimated at 0.5% for the original glass and a maximum of 2% for the TT ones.

sion decreases with increasing pressure. Beyond 7 MPa, the error is 1%. As the pressure enhances the contact of the sensors on the glass surface and, consequently, the quality of the measurements, we assume a conservative error of 1% for Figure 6a.

[22] The elastic wave velocities of the argon gas saturated sample show increasing values with increasing effective confining pressure, then tend to reach a plateau. The water saturated sample V_P remains stable in the same range of effective confining pressure but the V_S measurements show a small increase with increasing effective confining pressure. The water saturated sample presents higher velocity values (both for V_P and V_S) than the argon gas saturated sample. Both saturated samples show velocity data in between the velocity data measured in dry original and 300 TT glasses (Figure 6b).

[23] Under deviatoric conditions, we observed a preliminary stage during which the radial P wave velocity remains stable, while the axial P wave velocity increases a little (Figure 7a). Then, beyond 50 MPa of deviatoric stress, both axial and radial P wave velocities decrease similarly, with the difference increasing from 150 to more than 300 m/s at $\sigma_1 - \sigma_1 \sim 185$ MPa (axial velocities being always higher than radial velocities, as expected). Figure 7b shows the small velocity relaxations recorded simultaneously with the stress relaxation when the deviatoric stress was fixed at ~180 MPa.

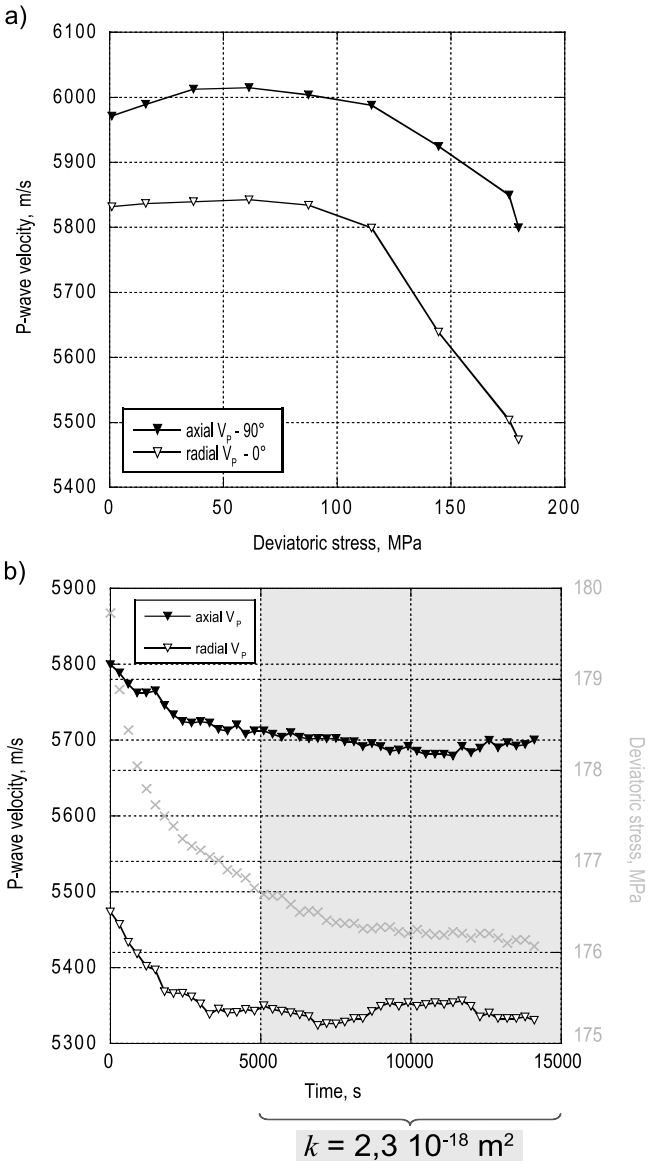

Figure 7. Damage monitoring of the argon gas saturated glass under deviatoric stress: (a) axial and average radial P wave velocity evolution during loading up to ~180 MPa of deviatoric stress and (b) P wave velocity relaxations following the axial stress relaxation during the time of the permeability measurements.

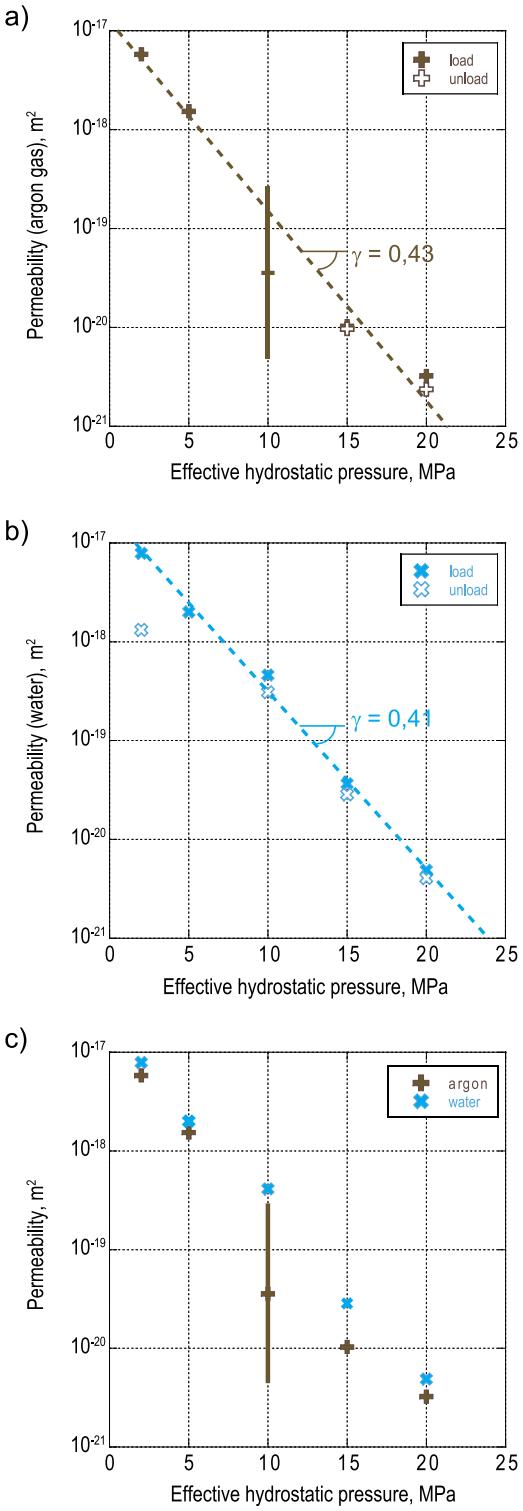

Figure 8. Permeability measurements under 300°C TT glasses in hydrostatic conditions: (a) permeability data during loading ($P_{effective}$ = 2 to 20 MPa) and unloading ($P_{effective}$ = 20 to 15 MPa) for the argon gas saturated sample, (b) permeability data for water saturated sample during loading ($P_{effective}$ = 2 to 20 MPa) and unloading ($P_{effective}$ = 20 to 2 MPa), and (c) permeability of argon gas and water tests during loading ($P_{effective}$ = 2 to 20 MPa).

After about one and a half hours of fixed deviatoric stress, the P wave velocities reach a plateau value where $V_P^{radial} \sim$ 5350 m/s and $V_P^{axial} \sim$ 5690.

3.2. Permeability of Cracked Glass

[24] Figure 8 shows the permeability measurements obtained during the two tests under hydrostatic conditions, performed on two different glass samples. The first saturated experiment was performed with argon gas, the second with mineral water. The cross size is representative of the uncertainty of each permeability value. As the pore pressure is fixed at 5 MPa, we refer to effective confining pressure $P_{effective}$ ranging from 2 to 20 MPa (*i.e.* $P_{hydrostatic}$ = 7 to 25 MPa).

[25] These data show several facts: (1) both the argon and water measurements are identical and (2) the decrease with increasing pressure is linear on a semilog plot. Note that the decrease is very large, slightly more than three orders of magnitude. At $P_{effective}$ = 2 MPa, the permeability value is about ~7 × 10^{-18} m^2. At $P_{effective}$ = 20 MPa, $k \sim 4.5 \times 10^{-21}$ m^2. The permeability value measured in the argon gas saturation test at $P_{effective}$ = 10 MPa has a large uncertainty (Figure 8a). This results from the use of the constant flow method at the limit of its applicability.

[26] Figure 8 data are consistent with a power or exponential law:

$$k = k_o e^{-\gamma P}, \tag{8}$$

where k_o is the initial permeability of the material at zero pressure. The coefficient γ is a constant of the material, independent of the fluid nature. It corresponds to the pressure sensitivity parameter first introduced by *Brace et al.* [1968]. From Figure 8, we derive γ = 0.42 ± 0.01 MPa^{-1} (Table 3).

[27] We also note that the permeability values measured with argon gas are very close to the permeability values measured with water (Figure 8c). This is consistent with a negligible Klinkenberg effect, as discussed above.

[28] In order to investigate the possible effect of mechanical damage on permeability, the effective pressure was fixed at 15 MPa (P_{pore} = 5 MPa with argon gas) and the deviatoric stress was increased to ~180 MPa. At this value, a significant damage is evident from the decreasing velocities (Figure 7a). The axial P wave velocity decreases of ~200 m/s and the radial P wave velocity decreases of ~400 m/s. The axial stress was held constant at ~200 MPa in order to measure the permeability (Figure 7b) with the steady state flow method over 4 hours. During that time, some small stress relaxation took place (from 185 to 176 MPa of deviatoric stress).

Table 3. Exponential Coefficient γ of Pressure Sensitivity and Critical Pressure $P_{critical}$ Graphically Measured on Figure 8[a]

	Argon	Water
γ, MPa^{-1}	0.43	0.41
k_o, m^2	8.9 10^{-18}	1.8 10^{-17}
R^2	0.99	0.99
$P_{critical}$, MPa	2.3	2.4

[a] $P_{critical}$ is defined as γ^{-1}. The validity of these parameters is quantified by the linear regression coefficient R^2.

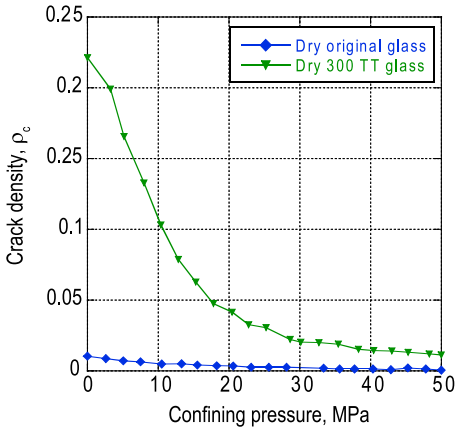

Figure 9. Crack densities calculated in dry 300°C TT glass and in the original glass samples, in dry condition under confining pressure.

[29] After the induced mechanical damage, permeability increased from 10^{-20} m^2 to 2.3×10^{-18} m^2. This latter value is close to the permeability measured at $P_{effective} = 2$ MPa (at the beginning of the hydrostatic loading). The deviatoric stress caused a permeability increase of over 2 orders of magnitude.

4. Discussion and Interpretation

4.1. Elastic Velocities and Crack Density

[30] Figure 6a, we showed the influence of fluids on the elastic parameters. These results can be compared to measurements on the original glass and the 300°C thermally treated dry glass in the same effective pressure range (Figure 6b, data from *Ougier-Simonin et al.* [2010]).

[31] The original glass has an almost perfect isotropic behavior, and shows the highest velocity values that were measured in this material, as expected.

[32] The velocity values measured in the dry TT glass (green curves on Figure 6) were the lowest. The increasing confining pressure induced the crack closure, as shown by the increasing velocity values. The saturated samples behavior is similar to the dry TT sample, with higher velocity values. All the TT samples, dry and saturated, tended to reach a velocity plateau, close to the original glass value. Finally, we note that the fluid presence enhanced this effect, allowing for the saturated glasses to reach the plateau value at a lower pressure than the dry TT glass. Note also that *S* wave velocities, and not just *P* wave values, are affected by the fluid.

[33] Figure 6 shows average values of *P* and *S* wave velocities along different paths. Crack closure is expected as the pressure increases [*Walsh*, 1965], and as a consequence the anisotropy due to crack distribution decreases. Using the isotropic moduli means in fact that the symmetry group (here transverse isotropy) is projected onto a subgroup (isotropic symmetry). Instead of using 5 elastic constants, we use 2 combinations of them [*Ougier-Simonin et al.*, 2009].

[34] Cracks are generally characterized by their very small aspect ratio (very small aperture compared to their length). We model the crack density following *Sayers and Kachanov* [1995] and *Sayers* [1999] assuming penny-shaped cracks homogeneously distributed in a homogeneous medium. The crack displacement discontinuity $[u_i]$, a measure of the relative displacement through a crack, is mathematically related to the stress field σ_{jk} by

$$[u_i] = B_{ij}\ \sigma_{jk}\ n_k \tag{9}$$

and

$$B_{ij} = B_N\ n_i n_j + B_T\ \left(\delta_{ij} - n_i n_j\right), \tag{10}$$

where n_k is the normal unit vector of the discontinuity, δ_{ij} is the Kronecker symbol, and B_N and B_T are the normal and shear component of B_{ij}, respectively. For open penny-shaped cracks with radius c in a homogeneous background medium (glass matrix here) with Poisson's ratio ν_o and Young's modulus E_o, in the case of dry cracks:

$$B_N = 16\left(1-\nu_o^2\right)\frac{c}{3\pi E_o}, \tag{11}$$

$$B_T = 32\left(1-\nu_o^2\right)\frac{c}{3\pi E_o(2-\nu_o)}. \tag{12}$$

The additional elastic compliance induced by the crack presence in an isotropic matrix is then [*Sayers and Kachanov*, 1995]

$$\Delta S_{ijkl} = \frac{32\left(1-\nu_0^2\right)}{3(2-\nu_0)E_0} \times \left[\frac{1}{4}\left(\delta_{ik}\alpha_{jl} + \delta_{il}\alpha_{jk} + \delta_{jk}\alpha_{il} + \delta_{jl}\alpha_{ik}\right) - \frac{\nu_0}{2}\beta_{ijkl}\right]. \tag{13}$$

With the second rank tensor α_{ij} and the fourth rank tensor β_{ijkl} [*Kachanov*, 1994], we write the specific contribution of the crack presence to additional elastic compliance as

$$\Delta S_{ijkl} = h\left[\frac{1}{4}\left(\delta_{ik}\alpha_{jl} + \delta_{il}\alpha_{jk} + \delta_{jk}\alpha_{il} + \delta_{jl}\alpha_{ik}\right) + \psi\beta_{ijkl}\right], \tag{14}$$

where

$$h = \frac{32\left(1-\nu_0^2\right)}{3(2-\nu_0)E_0}, \tag{15}$$

$$\psi^{\mathrm{dry}} = \frac{-\nu_0}{2} \text{ or } \psi^{\mathrm{sat}} = -1, \tag{16}$$

$$\alpha_{ij} = \frac{1}{V_r}\sum\left(c^3 n_i n_j\right)^{(r)}, \tag{17}$$

and

$$\beta_{ijkl} = \frac{1}{V_r}\sum\left(c^3 n_i n_j n_k n_l\right)^{(r)}, \tag{18}$$

r representing the rth penny-shaped crack. The crack density parameter ρ_c in the transverse isotropic symmetry naturally appears to be the linear invariant $tr(\alpha_{kk}) = \rho_c = Nc^3/V$.

[35] The ρ_c values (Figure 9) have been calculated from the experimental velocity data for the original glass and the dry 300°C TT glass in the pressure range 0 − 50 MPa [*Ougier-Simonin et al.*, 2010]. The crack density in the original glass is zero, as expected. The slight decrease observed at

very low pressure is due to an experimental artifact (transducer contact on the glass surface). The crack density in the thermally treated glass decreases from ρ_c = 0.22 to 0.04 between 0 and 20 MPa confining pressure, then from ρ_c = 0.04 to 0.015 between 20 and 50 MPa. Thus crack density decreases most rapidly at pressures below 20 MPa.

[36] We have assumed a homogeneous distribution of cracks whereas we know that cracks are mostly present in an external ring (see section 2.3) of thickness equal to about 15% of the cylinder radius. In order to take this fact into account, we can consider that the measured crack density ρ_c is an apparent one. We should substitute for it a density ρ'_c that is higher but exists only in the external ring. This ring is limited by the cylinder radius r and a smaller radius r' such as r'/r = 0.85. Accounting for this implies that ρ'_c is higher than ρ_c by a factor close to 4 (i.e. volume ratio $V_{cylinder}/V_{ring}$).

4.2. Characterization of the Thermally Induced Crack Population

[37] The closure stress σ_{close} at which cracks close is [*Walsh*, 1965; *Jaeger et al.*, 2007]

$$\sigma_{close} = \frac{\pi\xi E}{4(1-\nu^2)} \approx \xi E, \tag{19}$$

where E is the Young modulus (GPa), ξ the mean crack aspect ratio and ν the Poisson's ratio. The crack aperture w is expected to vary under pressure [*Jaeger et al.*, 2007]:

$$w = w_o\left(1 - \frac{P}{b}\right), \tag{20}$$

and $b \approx E\xi$.

[38] Using these relations and the experimental results from Figure 6a, we calculate $10^{-4} \leq \xi < 10^{-3}$ for the thermally induced cracks at 300°C (E = 71.7 ± 5 GPa and ν_{300TT} = 0.28 ± 3). SEM observations (Figure 1) indicate a mean crack length $c \sim 500$ μm. Recalling that $\xi = w/c$, we calculate an initial average aperture of w_o = 0.1 μm.

4.3. Permeability

[39] According to *Dienes* [1982] and *Guéguen and Dienes* [1989], the permeability k of a cracked material with an isotropic distribution of the crack population can be written as

$$k = \frac{2}{15} f w^2 \xi \rho_c, \tag{21}$$

where ξ is the crack aspect ratio, ρ_c the crack density and w the average crack aperture. The connectivity f represents the crack fraction that are hydraulically connected and can be determined with the percolation theory. Note that for anisotropic crack distribution, the percolation threshold is close to ρ_c = 0.1 [*Guéguen and Dienes*, 1989]. If we can determine ξ and ρ_c (through the elastic moduli measurements), then measurement of k leads directly to that of w [*Fortin et al.*, 2010].

[40] Assuming an isotropic crack distribution, velocity data at 7.5 MPa confining pressure are consistent with ρ_c = 0.13 (Figure 9). Consequently, the percolation threshold should occur at $P_{confining}$ = 7.5 MPa and the permeability should be zero beyond that. However, Figure 8 shows that permeability is nonzero up to $P_{confining}$ = 20 MPa. This emphasizes that the crack orientation distribution is not isotropic. This observation is consistent with the velocity data and the numerical modeling (Figure 3). During the thermal shock, the maximum stress is $\sigma_{\theta\theta}$ (Figure 3) which implies that the crack distribution should not be isotropic. It should be dominated by vertical cracks. Consequently, the percolation threshold for vertical flow is expected to be reached at lower crack density values. Isotropic percolation does not apply in our case.

[41] As discussed in section 4.1, we have assumed an homogeneous distribution of cracks whereas we know that most cracks are within the external sample ring. The consequence is that the measured vertical permeability is an *apparent* permeability, lower than that of the external ring (which is around 4 times higher).

[42] We assume in the following that cracks are connected in the vertical (axial) direction, and that permeability is a function of crack density and crack aperture. Since crack aperture is the key parameter for permeability in our case, we can use a modified form of equation (21) and write

$$k = m w^2 \phi, \tag{22}$$

where m is the connectivity factor assuming to be about 1. The crack porosity is

$$\phi = 2\pi c^2 w N, \tag{23}$$

with N the total number of cracks per unit volume. Then

$$k = m\pi c^2 w^3 N, \tag{24}$$

or, using $\rho_c = Nc^3$,

$$k = m\pi\rho_c \xi w^2. \tag{25}$$

At an effective confining pressure of 5 MPa, $k \sim 2 \times 10^{-18}$ m^2, ρ_c = 0.2 (Figure 9) and $\xi = 5 \times 10^{-4}$ ($10^{-4} \leq \xi < 10^{-3}$), therefore the average crack aperture, w, is around 0.2 μm, a value consistent with the one obtained from the velocity data (section 4.2).

[43] As the crack radius is not sensitive to pressure P, only w varies under pressure. This leads to $k \propto w^3$ from equations (21) or (25), the cubic relation between the permeability and the crack aperture. Using (8) and (20)

$$k_o e^{-\gamma P} \propto w_o^3\left(1 - \frac{P}{b}\right)^3 \tag{26}$$

and $b \sim \xi E$. For P = 0, $k_o \propto w_o^3$. Thus,

$$-\gamma P \propto 3\log\left(1 - \frac{P}{b}\right). \tag{27}$$

Then, for $P/b \ll 1$, this leads to

$$\gamma \sim \frac{3}{\xi E}. \tag{28}$$

Using the Young modulus value measured in ambient conditions (no pressure, temperature, or fluid) on the 300 TT

Table 4. Compilation of Published Data on the Pressure Sensitivity of Permeability for Different Low Porosity Rocks

Reference	Rock Type	γ (10^{-2} MPa^{-1})	σ^* (MPa)
Yale [1984]	tight sandstones	3.8 − 6.3	15.9 − 26.3
Brace et al. [1968]	Westerly granite	3.3	30.6
Bernabé [1986]	Chelmsford granite	2.9	34.6
	Barre granite	2.3	42.7
Fisher and Paterson [1992]	Carrara marble	4.7	21.3
Morrow et al. [1994]	Gneiss (Kola)	3.2	31.2
	basalt (Kola)	10.2	9.8
	amphibolite (KTB)	5.8 − 11.0	9.1 − 17.2
Fortin et al. [2010]	basalt (Etna)	0.025 − 0.06	16.7 − 40
This study	synthetic borosilicate glass	40	2.3

glass (Table 1) and $\gamma = 0.4$ MPa^{-1} (Table 3), we calculate $\xi \sim 10^{-4}$ from equation (28). This result, obtained independently using permeability measurements, is consistent with the crack aspect ratio estimated from the elastic wave velocities and the crack closure stress. Therefore we conclude that the permeability is controlled by the flow evolution through cracks with an aspect ratio of 10^{-4}. Because we consider above the relative variation of k with P, the question of apparent versus real crack density does not matter here.

[44] This crack aspect ratio value is a result of the very sharp tip of the cracks in glass, as there are no crystal structure and no grain boundaries. The crack tips in glass are only controlled by nanoscale defects on the scale of the rugosity in glass. This sharp form is expected to be very sensitive to pressure and this is very consistent with our results (both elastic and transport properties). The permeability data reported on Figure 8 shows this trend: the confining pressure closes cracks [*Walsh*, 1965; *Mavko et al.*, 1998], with a very high parameter sensitivity factor γ.

[45] Finally, as reported in section 3, mechanical damage increases the permeability by slightly more than 2 orders of magnitude. This results from (1) either crack density increase or (2) from crack aperture increase, or both. The elastic wave velocity decrease (Figure 7) points to the first effect, an increase of ρ_c. However, this is not sufficient to explain the permeability jump. The crack density increase is less than a factor 10, whereas the permeability increase is over 100. It can be concluded that the increase in crack aperture is the dominant effect.

4.4. Glass Versus Rocks

[46] We see from Table 4 that γ values reported here for glass are much higher than those reported for rocks [*Yale*, 1984; *Bernabé*, 1986; *Huenges and Will*, 1989; *Fisher and Paterson*, 1992; *Morrow et al.*, 1994; *David et al.*, 1994]. The characteristic pressure for the exponential law $k(P)$ is only 2.4 MPa here for the glass whereas it is much higher for rocks. There are many reasons why this is to be expected: rocks have a grain structure, cracks in rocks may have experimented alteration, shear displacement, etc. But since cracks are smoother in glass than in rocks where they present asperities, we assume that this difference of rugosity could explain the factor value.

[47] Note also that the data obtained during unloading were similar to the loading values, both for argon and water saturated conditions. This implies that the effect is reversible, and suggests elastic closure and reopening of smooth cracks. *Fortin et al.* [2010] also observed this reversibility in basalt, which has a texture similar to that of glass. For softer rocks such as clay sandstones, creep may lead to irreversible crack deformation. This observation allows us to interpret the glass permeability properties as a good analogue to those of basalt.

5. Conclusions

[48] A detailed investigation of cracked glass samples under pressure has been conducted using thermally treated glasses at 300°C. Our results have shown that (1) the thermal treatment has induced an averaged (apparent) crack density up to 0.2 in the samples, (2) mean crack aspect ratio is in the range of 10^{-4} to 10^{-3}, (3) permeability decreases as a function of pressure following a power law (exponential), (4) permeability depends on the crack aperture cube, and (5) permeability behavior is reversible and independent of the fluid nature.

[49] Two independent methods (permeability and elastic wave velocity measurements) give consistent results for the mean crack aspect ratio and the mean crack aperture.

[50] These experimental results are of interest for two reasons. First, this investigation provides data on the mechanical and transport properties of an almost ideally brittle elastic solid, representing the end-member behavior of crack effects in real rocks, both for the crack effect on velocities [see, e.g., *Sayers and Kachanov*, 1995; *Schubnel and Guéguen*, 2003; *Vinciguerra et al.*, 2005; *Benson et al.*, 2006a; *Fortin et al.*, 2007] and permeability [*Guéguen and Dienes*, 1989; *David et al.*, 1994; *Fortin et al.*, 2010]. Considering the crack effect, the assumption done for rocks fits well the idealized view of cracks. Crack permeability results in rocks should be carefully compared to the thermally treated glass permeability since crack asperities may affect its evolution under pressure. Second, if vitrified nuclear waste contains cracks, it is important to know the response of the cracks to pressure. Our results imply that cracks with an aspect ratio of about 10^{-4} should close at a lithostatic pressure of 15 MPa.

[51] When subjected to pressure in water saturated condition during a long time, cracked glass may exhibit a lower mechanical resistance to failure. Over timescale of our experiments, we saw no evidence for subcritical processes. Further study of slow crack effect in this glass appears thus to be interesting both to investigate the stress corrosion for nuclear safety disposal model and to quantify the time to failure response of an almost ideal elastic brittle solid (following, for instance, *Wiederhorn* [1966] and *Anderson and Grew* [1977]). To our knowledge, no study performing permeability measurements in borosilicate thermally treated glass cylinder under triaxial stresses has ever reported such

data. Further study should also complement long time effects with regard to possible devitrification (following, for instance, *Wiederhorn and Johnson* [1973], and more recently *Frugier et al.* [2008]). The expected behavior is likely to be different in that case.

[52] **Acknowledgments.** The authors want to thank the French Atomic Energy Commision (CEA), AREVA NC, and French National Radioactive Waste Management Agency (l'ANDRA) for supporting this research work and for their fruitful discussions and advice. They are grateful for the help of the CEA laboratory for providing all SON68 samples. They also thank Pr. Yves Leroy from the Laboratoire de Géologie (ENS) for providing them with the Fortran program.

References

Adda-Bedia, M., and Y. Pomeau (1995), Crack instabilities of a heated glass strip, *Phys. Rev. E*, *52*, 4105–4113.

Anderson, O., and P. Grew (1977), Stress corrosion theory of crack propagation with applications to geophysics, *Rev. Geophys.*, *15*, 77–104.

Atkinson, B., and P. Meredith (1987), *The Theory of Subcritical Crack Growth With Applications to Minerals and Rocks*, Academic, London.

Benson, P., P. Meredith, and A. Schubnel (2006a), Modeling the permeability evolution of microcracked rocks from elastic wave velocity inversion at elevated isostatic pressure, *J. Geophys. Res.*, *111*, B04202, doi:10.1029/2005JB003710.

Benson, P., A. Schubnel, S. Vinciguerra, C. Trovato, P. Meredith, and R. Young (2006b), Role of void space geometry in permeability evolution crustal rocks at elevated pressure, *J. Geophys. Res.*, *111*, B12203, doi:10.1029/2006JB004309.

Bernabé, Y. (1986), The effective pressure law for permeability in chelmsford granite and barre granite, *Int. J. Rock Mech. Min. Sci. Geomech. Abstr.*, *23*, 267–275.

Bernabé, Y. (1987), A wide range permeameter for use in rock physics, *Int. J. Rock Mech. Min. Sci.*, *24*, 309–315.

Brace, W., J. Walsh, and W. Frangos (1968), Permeability of granite under high pressure, *J. Geophys. Res.*, *73*, 2225–2236.

Brown, R., and J. Korringa (1975), On the dependence of elastic properties of a porous rock on the compressibility of the pore fluid, *Geophysics*, *40*, 608–616.

David, C., T.-F. Wong, W. Zhu, and J. Zhang (1994), Laboratory measurement of compaction-induced permeability change in porous rocks: Implication for the generation and maintenance of pore pressure excess in the crust, *Pure Appl. Geophys.*, *143*, 425–456.

Dienes, J. (1982), *Permeability, Percolation and Statistical Crack Mechanics*, Am. Inst. of Min., Metal. and Pet. Eng., New York.

Falleti, D., and L. Ethridge (1988), A method for predicting cracking in waste glass canisters, *Nucl. Chem. Waste Manage.*, *8*, 123–133.

Fisher, G., and M. Paterson (1992), Measurement of permeability and storage capacity in rocks during deformation at high temperature and pressure, in *Fault Mechanics and Transport Properties of Rocks*, pp. 213-252, Academic, London.

Fortin, J., Y. Guéguen, and A. Schubnel (2007), Effects of pore collapse and grain crushing on ultrasonic velocities and v_P/v_S, *J. Geophys. Res.*, *112*, B08207, doi:10.1029/2005JB004005.

Fortin, J., S. Stanchits, S. Vinciguerra, and Y. Guéguen (2010), Influence of thermal and mechanical cracks on permeability and elastic wave velocities in a basalt from mt. etna volcano subjected to elevated pressure, *Tectonophysics*, *503*, 60–74, doi:10.1016/j.tecto.2010.09.028.

Frugier, P., et al. (2008), Son68 nuclear glass dissolution kinetics: Current state of knowledge and basis of the new graal model, *J. Nucl. Mater.*, *380*, 8–21.

Griffith, A. (1920), The phenomena of rupture and flow in solids, *Philos. Trans. R. Soc. London A*, *221*, 163–198.

Guéguen, Y., and J. Dienes (1989), Transport properties of rocks from statistics and percolation, *Math. Geol.*, *21*, 1–13.

Gueguen, Y., and V. Palciauskas (1994), *Introduction to the Physics of Rocks*, Princeton Univ. Press, Princeton, N. J.

Huenges, E., and G. Will (1989), Permeability, bulk modulus and complex resistivity in crystalline rocks, in *Fluid Movements, Element Transport and the Composition of the Deep Crust*, pp. 361–375, Kluwer Acad., Dordrecht, Netherlands.

Jaeger, J., N. Cook, and R. Zimmerman (2007), *Fundamentals of Rock Mechanics*, 4th ed., Blackwell, Malden, Mass.

Kachanov, M. (1994), Elastic solids with many cracks and related problems, *Adv. Appl. Mech.*, *30*, 259–445.

Kamizono, H., and M. Senoo (1983), Thermal shock resistance of a simulated high-level waste glass, *Nucl. Chem. Waste Manage.*, *4*, 329–333.

Kranz, R. (1983), Microcracks in rocks: A review, *Tectonophysics*, *100*, 449–480.

Kranz, R., A. Frankel, T. Engelder, and C. Sholz (1979), The permeability of whole and jointed barre granite, *Int. J. Rock Mech. Min. Sci. Geomech. Abstr.*, *16*, 225–234.

Lawn, B. (1993), *Fracture of Brittle Solids*, 2nd ed., Cambridge Univ. Press, New York.

Mavko, G., T. Mukerji, and J. Dvorkin (1998), *The Rock Physics Handbook*, Cambridge Univ. Press, Cambridge, U. K.

Morrow, C., D. Lockner, S. Hickman, M. Rusanov, and T. Röckel (1994), Effects of lithology and depth on the permeability of core samples from the kola and ktb drillholes, *J. Geophys. Res.*, *99*, 7263–7274.

Nara, Y., P. Meredith, T. Yoneda, and K. Kaneko (2010), Influence of macro-fractures and micro-fractures on permeability and elastic wave velocities in basalt at elevated pressure, *Tectonophysics*, *503*, 52–59, doi:10.1016/j.tecto.2010.09.

Nasseri, M., A. Schubnel, P. Benson, and R. Young (2009), Common evolution of mechanical and transport properties in thermally cracked westerly granite at elevated hydrostatic pressure, *Pure Appl. Geophys.*, *166*, 927–948.

O'Connell, R., and B. Budiansky (1974), Seismic velocities in dry and saturated cracked solids, *J. Geophys. Res.*, *79*, 5412–5426.

Ougier-Simonin, A., J. Sarout, and Y. Guéguen (2009), A simplified model of effective elasticity for anisotropic shales, *Geophysics*, *74*, D57–D63, doi:10.1190/1.3096616.

Ougier-Simonin, A., J. Fortin, Y. Guéguen, A. Schubnel, and F. Bouyer (2010), Cracks in glass under triaxial conditions, *Int. J. Eng. Sci.*, *49*, 105–121, doi:10.1016/j.ijengsci.2010.06.026.

Paterson, M., and T. Wong (2005), *Experimental Rock Deformation - The Brittle Field*, Springer, Berlin.

Perez, J., and J. Westsik (1981), Effects of cracks on glass leaching, *Nucl. Chem. Waste Manage.*, *2*, 165–168.

Pratt, H., H. Swolfs, W. Brace, A. Black, and J. Handin (1977), Elastic and transport properties of an in situ jointed granite, *Int. J. Rock Mech. Min. Sci. Geomech. Abstr.*, *14*, 35–45.

Sakaue, K., S. Yoneyama, and M. Takashi (2009), Study on crack propagation behavior in a quenched glass plate, *Eng. Fract. Mech.*, *76*, 2001–2024.

Sato, S., K. Asakura, and H. Furuya (1983), Microstructure of high-level radioactive waste glass heavily irradiated in a high-voltage electron microscope, *Nucl. Chem. Waste Manage.*, *4*, 147–151.

Sayers, C. (1999), Stress-dependent seimsic anisotropy of shales, *Geophysics*, *64*, 93–98.

Sayers, C., and M. Kachanov (1995), Microcracks-induced elastic wave anisotropy of brittle rocks, *J. Geophys. Res.*, *100*, 4149–4156.

Scholz, C. (1968), The frequency-magnitude relation of microfracturing in rock and its relation to earthquakes, *Bull. Seismol. Soc. Am.*, *58*, 399–415.

Schubnel, A., and Y. Guéguen (2003), Dispersion and anisotropy of elastic waves in cracked rocks, *J. Geophys. Res.*, *108*(B2), 2101, doi:10.1029/2002JB001824.

Spiers, C. J., J. L. Urai, G. S. Lister, J. N. Boland, and H. J. Zwart (1984), *Influence of Fluid-Rock Interaction on the Rheology of Salt Rock: Final Report*, Harwood, Reading, U. K.

Timoshenko, S. P., and J. N. Goodier (1970), *Theory of Elasticity*, 3rd ed., McGraw-Hill, New York.

Vinciguerra, S., C. Trovato, P. Meredith, and P. Benson (2005), Relating seismic velocities, thermal cracking and permeabillity in Mt. Etna and Iceland basalts, *Int. J. Rock Mech. Min. Sci.*, *42*, 900–910.

Walsh, J. (1965), The effect of cracks on the compressibility of rocks, *J. Geophys. Res.*, *70*, 381–389.

Wiederhorn, S. M. (1966), *Effects of Environment on the Fracture of Glass*, Gordon and Breach, New York.

Wiederhorn, S. M., and H. Johnson (1973), Influence of sodium-hydrogen ion exchange on crack propagation in soda-lime silicate glass, *J. Am. Ceram. Soc.*, *56*, 108–109.

Yale, D. (1984), Network modelling of flow, storage and deformation in porous rocks, Ph.D. thesis, Stanford Univ., Stanford, Calif.

F. Bouyer, CEA, Site de Marcoule DTCD/SECM, Bagnols-Sur-Cèze CEDEX F-30207, France.

J. Fortin, Y. Guéguen, A. Ougier-Simonin, and A. Schubnel, Laboratoire de Géologie, Ecole Normale Supérieure, CNRS, UMR 8538, 24 rue Lhomond, F-75005 Paris, France. (ougier@geologie.ens.fr)